High-Throughput Experimentation for Selective Growth of Small-Diameter Single-Wall Carbon Nanotubes using Ru-Promoted Co Catalysts

Brian M. Everhart,[1] Rahul Rao,[2] Pavel Nikolaev,[2] Tsung-Wei Liu,[3] Diego A. Gómez-Gualdrón,[3] Benji Maruyama,[2] Placidus B. Amama[1*]

[1]*Tim Taylor Department of Chemical Engineering, Kansas State University, Manhattan, Kansas 66506*

[2]*Materials and Manufacturing Directorate, Air Force Research Laboratory, WPAFB, Ohio 45433*

[3]*Department of Chemical and Biological Engineering, Colorado School of Mines, Golden, Colorado 80401*

[*] Corresponding author
P.B. Amama; E-mail: pamama@ksu.edu

Abstract

Small-diameter single-wall carbon nanotubes (SWCNTs) are desirable in a variety of applications requiring electronic bandgaps greater than 1 eV. Here we utilize an Autonomous Research System (ARES)—an automated, high throughput, laser-induced CVD system with in situ Raman spectral feedback—to study the role of Ru promotion of Co catalysts in the growth of small-diameter SWCNTs. By performing over 200 growth experiments in ARES with different feedstocks and extensive multi-excitation Raman spectroscopic characterization, we demonstrate that Ru-promoted Co catalyst nearly doubles the selectivity of small-diameter SWCNTs (diameters below 1nm) at 750°C in comparison to Co. At higher temperatures between 800 and 850°C, Ru stabilizes Co catalyst nanoparticles and increases the selectivity of small-diameter SWCNTs by almost a factor of three. Results reveal that SWCNT diameters are not only dependent on catalyst properties but also on the type of feedstock as selectivity towards small-diameter SWCNTs decreases in the following order: ethylene > acetylene > FTS-GP (Fischer-Tropsch synthesis gaseous product mixture). Density functional theory (DFT) calculations with 13- and 55-atom Co_xRu_y clusters (ranging from 0% to 22% Ru content) reveal increases in cluster cohesive energies (E_C) with Ru content, irrespective of the exact location of Ru atoms in the clusters. As these findings are indicative of increases in melting temperature and reduction in atom mobility with Ru content, they are consistent with the presence of ~10% Ru in our Co catalyst increasing sintering resistance, stability of small nanoparticles, and the observed high selectivity toward small-diameter SWCNTs.

1. Introduction

Owing to their high carrier mobility, semiconducting single-wall carbon nanotubes (SWCNTs) are well-suited as building blocks in a wide range of electronic applications from nanoscale transistors,[1-4] flexible electronics,[5-11] and chemical and biological sensors to clean energy harvesting and storage devices.[12-17] These applications require SWCNTs with band gaps larger than 1 eV. However, due to the inverse relationship between nanotube diameter and band gap, nominally semiconducting SWCNTs with large diameters feature small band gaps that in practice make them semi-metallic.[18] Indeed, based on theoretical calculations,[19] to obtain the desired larger than 1 eV band gap requires the SWCNT diameter to be less than 1 nm. The challenge is that SWCNT synthesis, using scalable methods such chemical vapor deposition (CVD) aided by conventional catalysts (Fe or Co supported on Al_2O_3), usually results in wide diameter distributions, with nanotubes ranging from 0.7 nm to 3 nm.[20-21] Moreover, approaches such as the growth of self-supporting vertically aligned SWCNTs (i.e., SWCNT carpets or forests) using conventional catalysts is particularly prone to producing SWCNTs that tend toward larger diameters. (> 1.5 nm).[22-25]

Although numerous post-processing techniques such as DNA wrapping,[26] density-gradient ultracentrifugation,[27] gel chromatography,[28] and aqueous two-phase extraction[29] have been proposed to effectively sort SWCNTs by diameter, these methods are low throughput and ultimately induce defects that degrade the nanotubes electronic properties. Therefore, to unleash the full potential of SWCNTs as components of electronic devices, a critical challenge that needs to be addressed is the development of reliable approaches for scalable selective synthesis of small-diameter, semiconducting SWCNTs (< 1 nm), as this would reduce the need for throughput-limiting postprocessing altogether.[30] The central strategy for reducing nanotube

diameter during CVD synthesis is to minimize the catalyst particle size. The hypothesis that drives this strategy is the intimate relationship between the catalyst particle and SWCNT structure growing from it. For instance, molecular simulations modeling SWCNT growth make visually apparent the correlation between nanoparticle and nanotube diameter.[31] Furthermore, the correlation between size of the catalyst particle and SWCNT diameter is also supported by several experimental studies.[21, 32-33]

One method of controlling catalyst size in general involves incorporating high-melting-point transition metals into the catalyst, either as a promoter or co-catalyst (bimetallic catalyst), to enhance catalyst stability by suppressing sintering. The efficacy of this strategy has been demonstrated in several heterogeneous catalytic reactions such as methane oxidation and Fischer Tropsch Synthesis (FTS).[34-41] Cui et al.[40] showed that a Mo promoter reduced sintering of Fe catalyst in FTS, resulting in high catalytic activity, while Cao et al.[34] found that the addition of Rh promoter enhanced the thermal stability of Pt nanoparticles. In other studies, the introduction of a Ru promoter has been demonstrated to reduce catalyst sintering in numerous catalytic processes.[35, 37-38, 41] The unique ability of high-melting-point transition metals to reduce catalyst sintering has been applied to CVD synthesis of small-diameter SWCNTs. The first work utilizing high-melting-point transition metal for growth of SWCNTs was the CoMoCAT process, which utilized Mo to reduce sintering of Co catalyst during gas-phase growth of SWCNTs via CO disproportionation.[33, 42] The CoMoCAT catalyst reduced the average SWCNT diameter by ~0.1 nm compared to SWCNTs produced from other well-established approaches such as the HiPCO process (0.81 nm vs. 0.93 nm). For alcohol CVD, Maruyama and coworkers demonstrated the use of the anchoring effect of Cu in Co-Cu bimetallic catalyst.[43] Despite successes in SWCNT synthesis, the wide parameter space of growth conditions has largely been unexplored to date.

As a result, the complex relationship between catalyst promotion, type of feedstock, SWCNT diameter, and growth temperature is still poorly understood.

In light of the breadth of parameters that affect CVD growth, rapid experimentation is a powerful tool for investigating favorable conditions that promote selective growth of small-diameter SWCNTs. Here we utilize an Autonomous Research System (ARES)—an automated, high throughput, laser-induced CVD system with in situ Raman spectral feedback—to probe the combined role of Ru as a catalyst promoter and type of feedstock in the growth of small-diameter SWCNTs using conventional feedstocks (ethylene and acetylene) and a gaseous product mixture from Fischer-Tropsch synthesis (FTS-GP),[25, 44-46] our new feedstock that offers potential for scale-up. We demonstrate through over 200 growth experiments that the deposition of 0.1-nm-thick Ru on a Co catalyst film (1nm total thickness) nearly doubles the selectivity of SWCNTs with diameters below 1nm as determined by multi-excitation Raman spectroscopy. Furthermore, Ru stabilizes Co catalyst particles at elevated temperatures, increasing the selectivity of small-diameter SWCNTs by almost a factor of three at temperatures between 800°C and 850°C in comparison to Co. A mechanistic understanding of the observed phenomenon has been developed with support from density functional theory (DFT), which attributes the reduced diameters to the increased cohesive energy of catalyst particles. Higher Ru amounts (20% and 100%) are also probed to develop a deeper understanding of the role of Ru in SWCNT growth. These findings clearly highlight the importance of Ru promotion of Co for small-diameter SWCNT growth, which opens the door for future applications requiring small diameter SWCNTs.

2. Experimental Section

2.1. Preparation of catalyst substrates

The substrates used for growth in ARES contain silicon micropillars fabricated by reactive ion etching. A substrate contains a 12×12 array of patches, each of which consists of a 5×5 array of 10-μm-diameter, 10-μm-high silicon pillars on an SiO_2 underlayer. The pillars were coated with an alumina layer (10 nm thick) by atomic layer deposition. Additional experiments were also performed using alumina deposited by ion beam sputtering (IBS/e) and the results are summarized in the Supporting Information. Substrates with the different catalysts (Co, Co-Ru and Ru) were deposited using IBS/e. For Co or Ru, a 1-nm-thick Co or Ru film was deposited on the alumina-coated layer, while for Co-Ru, a 0.9-nm-thick Co film was deposited followed by a 0.1-nm-thick Ru film (the thicknesses were adjusted accordingly for Co-Ru with 20 wt% Ru). A unique feature of ARES is that each pillar behaves as a microreactor and can be rapidly heated to the growth temperature within a fraction of a second due to the poor thermal conductivity of SiO_2 and the small thermal mass of the pillars. Further description of the ARES system is presented elsewhere.[47]

2.2. SWCNT growth in ARES

The ARES system (Figure 1) utilizes a high power (6 W, Verdi) laser (532 nm) that serves as the heat and Raman excitation sources. Each substrate contains several silicon micropillars (fabricated by reactive ion etching) that are thermally isolated by a silicon dioxide underlayer. During each growth experiment, a micropillar was heated to the growth temperature by regulating the laser power. The laser enables instantaneous heating of the micropillar and de-wetting of the catalyst film without requiring an annealing step. The temperature resolution is ±10-15 °C. Conventional carbon feedstocks (ethylene and 1% acetylene in helium) and our

recently developed feedstock (FTS-GP) were used for this investigation. FTS-GP has the ability to support high growth rate and exceptionally long catalyst lifetime.[25, 44-46] Over the duration of an experiment, growth rate, yield, and temperature can be monitored via in-situ Raman spectroscopy using the same laser for heating. Raman spectra were acquired every 5 s and experiments were allowed to progress until SWCNT growth seemed to terminate, which was evidenced by a plateauing of the intensity of the SWCNT Raman peak (G band). The red shift of the Raman peak frequency was used to estimate the growth temperatures. When the growth appears to have terminated, the temperature can be reduced before moving to the next micropillar on the substrate. Raman spectra were collected before and after growth on each micropillar, enabling baseline subtraction for examination of radial breathing modes (RBMs), G-band, and D-band.

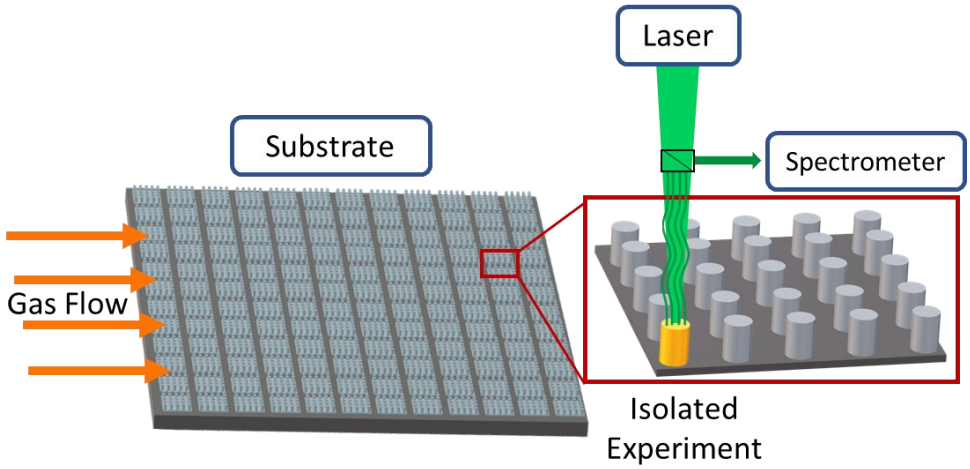

Figure 1. *Schematic illustration of ARES, a high throughput laser-induced CVD system capable of in-situ Raman spectroscopy.*

SWCNT growth is generally modeled by a self-exhausting exponential decay model (Equation 1) as the growth is characterized by a high growth rate at the beginning that subsequently diminishes until complete growth cessation occurs.[48] This model has been used in

previous studies for the analysis of SWCNT growth kinetics in ARES.[47, 49-53] The model used is given as

$$G(t) = \nu\tau\left(1 - e^{-\frac{t}{\tau}}\right) \quad (1)$$

where G represents area under the G-band at various times, t, while fitting parameters ν and τ represent the initial growth rate and catalyst lifetime, respectively.

Ex-situ Raman characterization of growth products was performed with a Renishaw InVia Raman microscope with a 633 nm excitation source for all pillars. In addition, multi-excitation Raman characterization was performed on selected pillars using 514, 633, 785, and 1064 nm excitation lasers. These additional laser excitations allow the measurement of the majority of the chiralities grown by CVD. The ex-situ Raman spectra also allowed for improved analysis of the RBMs due to the smaller spot size when compared to those obtained in ARES (1 μm vs. 10 μm). Each pillar was analyzed via a 10×10 array of spectra collected over the entire surface of the pillar. The 100 spectra collected were averaged and the resulting spectrum was analyzed, providing representative RBM data on the surface of each pillar. The combined use of Raman data collected from the 532 nm laser (ARES) and 633 nm laser (Renishaw) in our analysis increased our data integrity and reliability of our findings. The morphology and density of SWCNTs grown on the pillars were further characterized with a Hitachi S5200 field-emission scanning electron microscope (SEM) operated at 5 kV.

Statistical analysis was performed on the Raman data to demonstrate the difference in selectivity toward small-diameter SWCNTs for growth on Co and Co-Ru catalysts. Variables considered include excitation wavelength (532 nm vs. 633 nm excitation), catalyst type (Co vs. Co-Ru), and growth temperature range (650 – 699°C, 700 – 749°C, 750 – 799°C, and 800 –

850°C). Weighted average RBM values were calculated by summing the products of the integrated peak area for each RBM and the peak location, and dividing by the sum of the peak areas. Error bars have been included to show standard deviation. The average selectivity towards small-diameter SWCNTS for each experiment performed at each temperature range was calculated for each catalyst and Raman excitation wavelength. The average selectivity values at Raman excitation wavelengths of 532 nm and 633 nm were subsequently averaged to be more representative of the small-diameter SWCNT selectivity at each temperature range for the respective catalysts. In total, over 300 unique data points were analyzed. Comparison of the selectivity of Co and Co-Ru was performed by averaging the previously calculated values across all temperature ranges. Analysis of SWCNT diameter selectivity for the different feedstocks was also calculated and included in the Supporting Information.

2.3. Computational analysis methods

Spin-polarized, plane-wave density functional theory (DFT) cluster optimizations were performed using the Vienna ab initio simulation package (VASP 5.4.1).[54-56] The plane wave basis set to construct the solution to the Kohn-Sham equations was built using an energy cutoff of 400 eV. Electronic and atomic structure were solved using an iterative procedure, with the electronic structure for a given geometry was considered solved when the energy difference for the electronic structures of two consecutive iterations was lower than 10^{-4} eV. The geometry was considered optimized once the energy difference for the geometries of two consecutive iterations is lower than 10^{-3} eV. The generalized-gradient approximation (GGA) functional, Perdew-Burke-Ernzerhof (PBE)[57] was used to model electron exchange and correlation. Dispersion forces were modeled explicitly using the D2 correction by Grimme.[58] The core electrons were modeled using the projected-augmented wave method (PAW).[59-60] During the optimizations, 13-atom or 55-

atom clusters were placed at the center of an orthorhombic 30 Å × 31 Å × 32 Å supercell, and calculations were made at the gamma point, with Gaussian smearing using a 0.03 smearing parameter.[61] The cluster sizes for this study were selected for their highly symmetric and stable structures, and diameter within the range of interest for the experimental work.[62]

3. Results

3.1. SWCNT growth in ARES using different feedstocks

Raman spectra collected in situ during SWCNT growth in ARES were used to probe the diameter distributions. The RBM regions, between 100 and 360 cm^{-1}, were deconvoluted with several peak components (Lorentzian) to obtain peak frequencies. Representative Raman spectra and peak fitting of the RBM peaks for SWCNTs grown on Co and Co-Ru are shown in Figure S1. Figures 2a-c show the weighted average RBM values as a function of temperature for Co and Co-Ru using 532 nm and 633 nm laser excitations as well as the combined average of the two datasets.

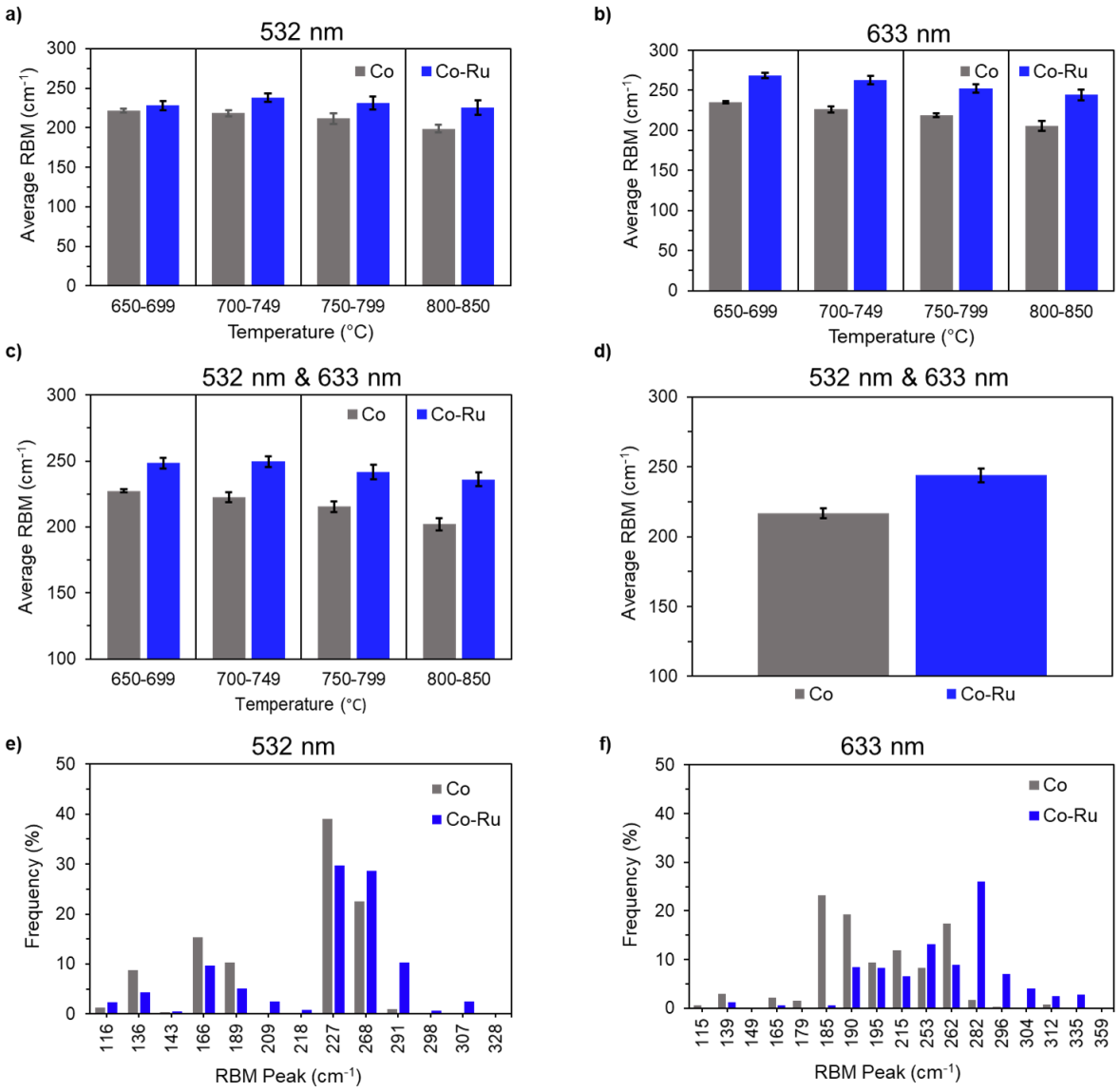

Figure 2. *Weighted average RBM frequency data acquired with 532 nm (a) and 633 nm (b) laser excitations at different growth temperature. (c) Approximation of the true RBM frequency distribution in each temperature bracket by averaging data in (a) and (b). (d) Mean of weighted average RBM frequency data in (c) for Co and Co-Ru. Histograms of relative frequency of RBM peaks as a function of peak location for Co and Co-Ru using 532 nm (e) and 633 nm (f) laser excitations; the relative frequency is the percentage of each RBM peak area to the total RBM peak area.*

Analysis of the Raman spectra acquired with 532 nm and 633 nm excitations (summarized in Figure 2) indicates growth on Co-Ru results in RBM peaks with significantly higher frequencies (corresponding to smaller SWCNT diameters) relative to growth on Co at all growth temperature ranges evaluated. While average RBM frequencies decrease with increasing temperature, Co-Ru is much less temperature dependent than Co (Figures 1a -c). The average RBM frequency for Co in the temperature range of 650-699 °C is 227 cm^{-1}, but decreases to 202 cm^{-1} at a higher temperature range (800-850 °C). On the other hand, growth on Co-Ru results in average RBM frequencies of 249 cm^{-1} and 236 cm^{-1} in the lowest and highest temperature ranges, respectively. Figure 2d shows the average RBM frequency for Co and Co-Ru obtained by averaging data in Figure 2c. Co-Ru exhibits a higher average RBM frequency (244 cm-1) than Co (217 cm^{-1}). Figures 2e and f show the average RBM components for all experiments performed on Co and Co-Ru using both laser excitations. It is clear from the histograms that spectra associated with Co-Ru have much higher relative frequency of RBM peaks corresponding to small SWCNT diameters, including a significant increase in RBMs > 290 cm^{-1}, which are almost non-existent for growth on Co. It should be noted that these RBM peak positions fluctuate +/- 3 cm^{-1} from spectra to spectra and likely represent several RBMs each. Additional analysis of RBM frequencies, including their analysis as a function of growth temperature and type of feedstock is summarized in Figures S2-S4.

It has been well established that RBM frequencies of SWCNTs are diameter dependent.[63-72] The following equation can be used to approximate SWCNT diameters from RBM peaks:

$$\omega_{RBM} = \frac{C_1}{d} + C_2 \quad (2)$$

where C_1 and C_2 are constants. Based on SEM evidence of the formation small tube bundles in our work, SWCNT diameters were calculated using $C_1 = 234$ and $C_2 = 10$.[66, 69] Detailed analysis of Equation 2 is included in the Supporting Information including the effects of SWCNT diameter, bundling interactions, and bundle size on appropriate C_2 values.

Selectivity of the catalysts toward growth of small-diameter SWCNTs was calculated from the fraction of the integrated intensities of all peak components below a diameter of 1 nm to the total integrated intensity of all fitted peak components in the RBM region between 100 and 360 cm^{-1} (Equation 3):

$$Selectivity = \frac{\text{Integrated area of RBM peaks corresponding to} < 1\text{nm}}{\text{Total integrated area of all RBM peaks}} \quad (3)$$

Representative SEM images of SWCNT bundles grown on pillars coated with Co and Co-Ru catalysts using ethylene as a feedstock reveal uniform growth across the entire catalyst surface with a higher density of SWCNTs grown on pillars coated with Co catalyst (Figure 3a) than pillars with Co-Ru catalyst (Figure 3b).

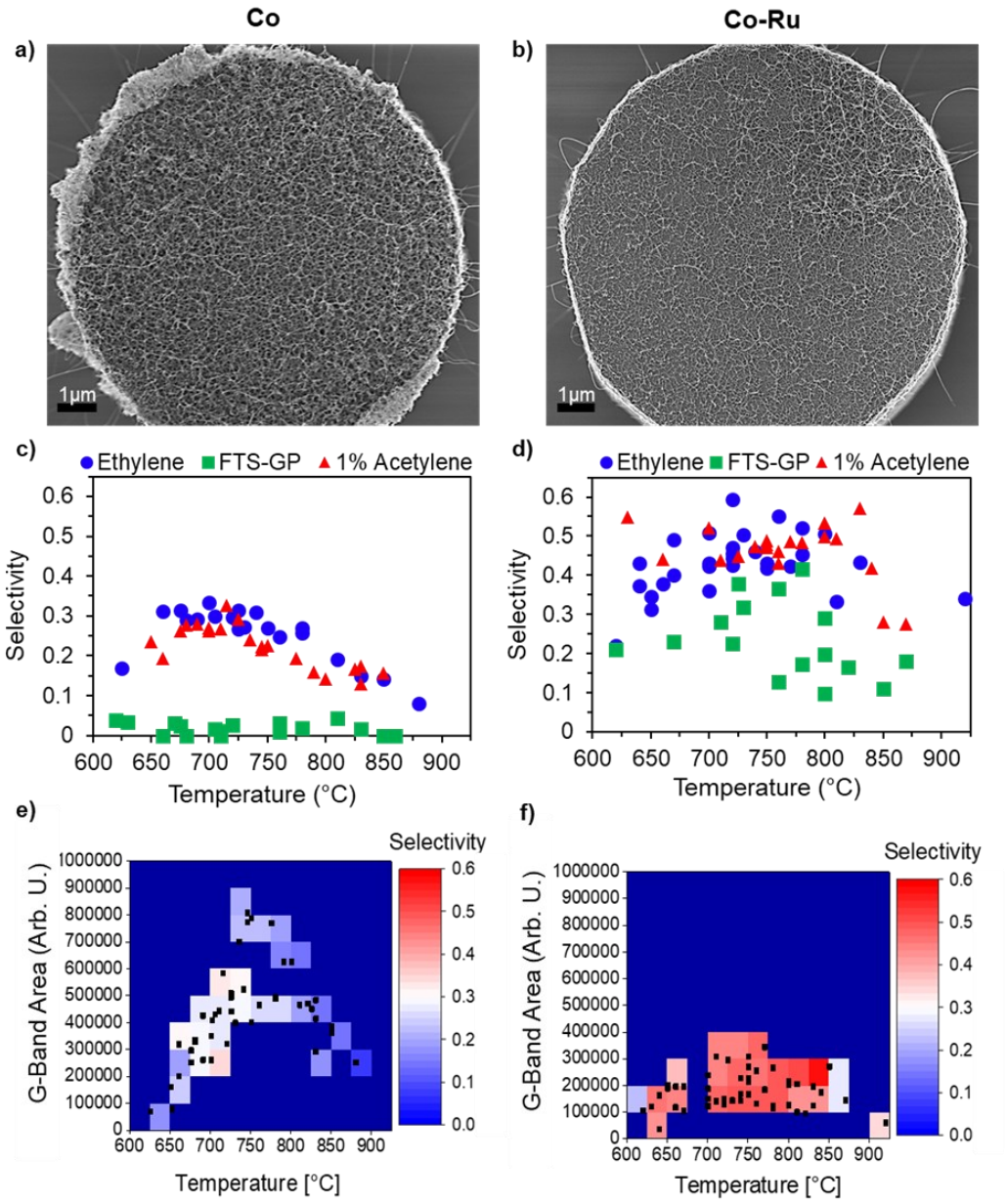

Figure 3. *SEM images showing density of SWCNTs grown on Co (a) and Co-Ru (b) catalysts. Plots of selectivity toward small-diameter SWCNTs as a function of growth temperature using different feedstocks on Co (c) and Co-Ru (d) catalysts (calculated from Raman spectra acquired with 532 nm laser excitation). Heat/contour plots illustrating selectivity (in c and d) and G-band area (proxy for abundance of SWCNT growth) versus growth temperature for Co (e) and Co-Ru (f) catalysts using growth results for ethylene and acetylene.*

Figure 3 (c-d) shows calculated selectivity toward small-diameter SWCNTs grown on Co and Co-Ru as a function of growth temperature for the different feedstocks (ethylene, FTS-GP, and acetylene) obtained using an excitation wavelength of 532 nm; the selectivity calculated from spectra obtained with 633 nm laser excitation are shown in Figure S5. SWCNTs grown on Co catalyst using ethylene or acetylene as a feedstock exhibited a maximum selectivity of 0.35 at ~700°C, whereas growth on the same catalyst using FTS-GP showed substantially lower selectivity (≤ 0.05) at all temperatures. On the other hand, SWCNTs grown on Co-Ru reached a maximum selectivity of 0.6 for ethylene, 0.57 for acetylene, and 0.42 for FTS-GP. It is evident from these results there is improved selectivity toward growth of small-diameter SWCNTs on Co-Ru catalyst even with FTS-GP as the feedstock. A clear trend of the scatterplots emerges for pure Co (using either acetylene or ethylene) with selectivity initially increasing with growth temperature from 600°C and peaking around 725°C and then decreasing with further increase in temperature. Using Ru as a catalyst promoter resulted in scattered selectivity data at the different temperatures; unlike acetylene, the trend that emerges for ethylene and FTS-GP is somewhat similar to that observed when Co catalyst is used. The spread in the data when Ru is present may be attributed to several factors including reduced density of tube nucleation and non-uniformity in the distribution of Ru in individual catalyst nanoparticles. The latter may lead to a slightly wider distribution of catalyst sizes that are comparatively smaller in size than those formed on Co. It is clear from these results that selectivity towards small-diameter SWCNTs decreases in the following order: ethylene > acetylene > FTS-GP. The effects of different values of C_1 and C_2 on the selectivity are summarized in Figure S6. Further analysis of selectivity using ethylene and acetylene (Figure S7) shows the higher small-diameter selectivity of ethylene over acetylene and Co-Ru over Co.

To compare the catalyst activity (in terms of SWCNT yield) and SWCNT diameter selectivity of Co and Co-Ru catalysts, heat plots showing selectivity to small-diameter SWCNTs (adapted from Figure 3 (c) and (d)) and SWCNT yield (or density) as functions of growth temperature as shown in Figure 3e and f. The analysis focuses on experiments utilizing ethylene and acetylene as feedstocks due to their overall high selectivity toward small-diameter SWCNTs. The integrated intensity of the G-band from the Raman spectrum collected at the end of each growth is used as a proxy for the yield of SWCNTs deposited on the catalyst-coated pillars. The SWCNT yield obtained from the G-band signal in ARES was verified by SEM and is consistent with previous studies.[44, 49-50] The SWCNT structures were not characterized by TEM due to the challenge associated with removing SWCNTs from individual micropillars without destroying the pillars and contaminating the SWCNT samples. Growth conditions favorable for high yield of small-diameter SWCNTs can be discerned from the heat plots. Growth on Co catalyst yielded SWCNTs with a maximum G-band area of ~8.0×10^5, but with a selectivity ~0.2; whereas growth on Co-Ru resulted in a lower maximum G-band area of ~3.5×10^5, but with a much higher selectivity ~0.4. The maximum yield on Co catalyst occurs at temperatures between 725 and 775°C, which is higher than the temperature range that supports the highest selectivity toward small-diameter SWCNTs (675 – 725°C, Figure 3c). In contrast, for Co-Ru catalyst, both SWCNT yield and selectivity were maximized at a temperature range of 725 – 775°C. We note that the maximum selectivity achieved for growth on Co-Ru is nearly twice that achieved on Co alone, whereas SWCNT yield on Co was two times higher than that on Co-Ru catalyst; this increased selectivity supports the hypothesis that the presence of Ru increases sintering resistance of catalysts and decreases the formation of large particles, and thus the yield of large-diameter SWCNTs. We conclude that using ethylene or acetylene as a feedstock under a

temperature range of 700-750°C favors the growth of small-diameter SWCNTs with Co-Ru being more selective and Co more active in terms of SWCNT yield.

To further understand the effect of Ru on catalytic activity during SWCNT growth, we fitted the growth curves at different growth temperatures for the various feedstock-catalyst combinations (Figures 4 a-d) to Equation 1: (a) ethylene and Co, (b) ethylene and Co-Ru, (c) acetylene and Co, and (d) acetylene and Co-Ru. The goodness of fit (R^2) for the analysis involving data from 20 experiments had an average value of 0.98. Figures 4e and f along with the average values of the fitting parameters (v and τ), summarized in Table S1, suggest that the presence of Ru increases the growth rate of SWCNTs, but with a decreased catalyst lifetime. Conversely, for pure Co a longer catalyst lifetime and lower growth rate are observed. The optimum temperature whereby catalyst lifetime and growth rate are maximized for both Co and Co-Ru is ~750°C.

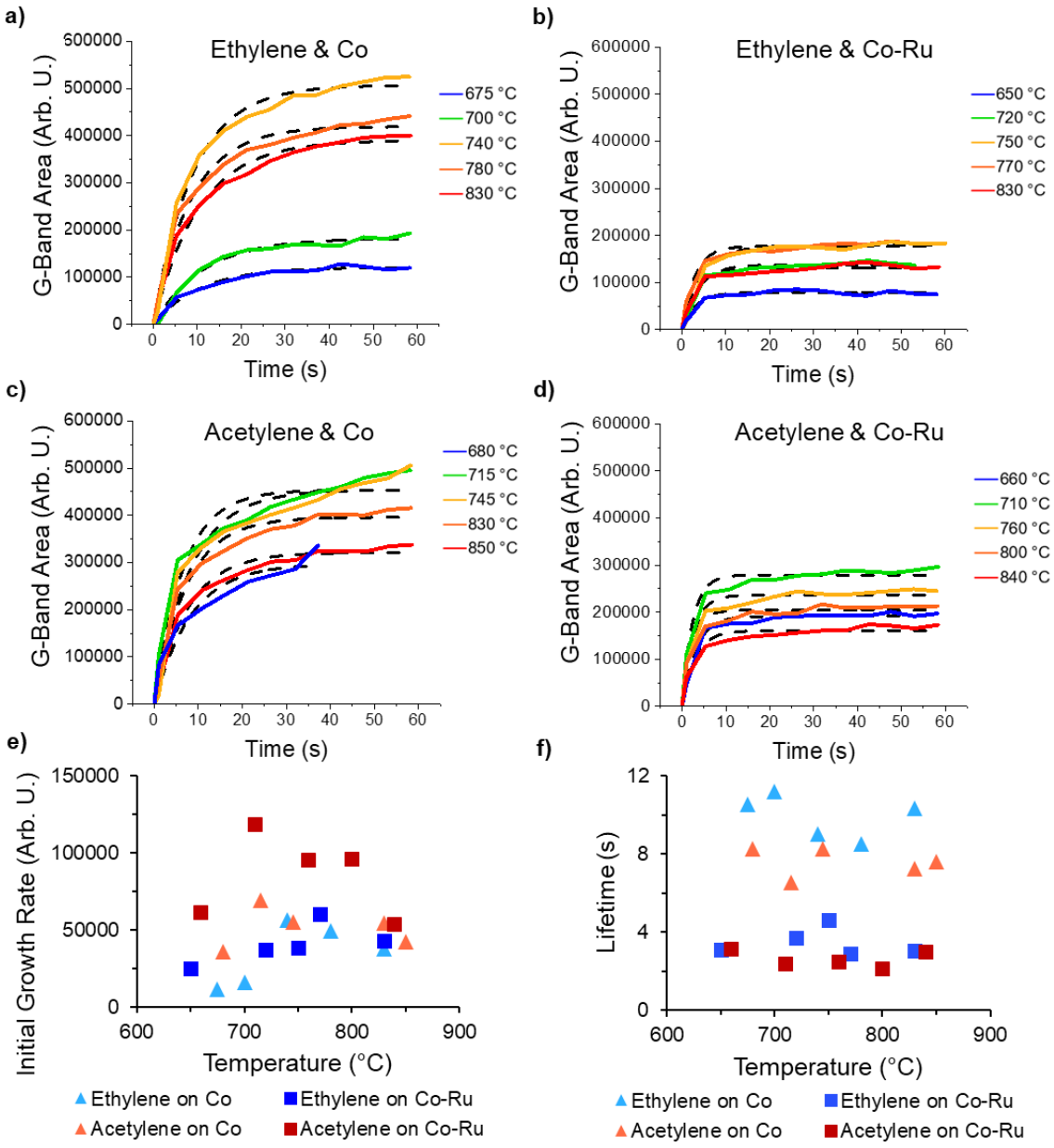

Figure 4. *Plots of SWCNT yield as a function of growth time using different feedstock-catalyst combinations: (a) ethylene and Co, (b) ethylene and Co-Ru, (c) acetylene and Co, and (d) acetylene and Co-Ru. The solid lines represent curve fitting of the radioactive decay model (Equation 1). Scatter plots of initial growth rate (e) and catalyst lifetime (f), obtained by fitting plots a-d to Equation 1, as a function of growth temperature.*

3.2. Multi-excitation Raman spectroscopic characterization of SWCNTs grown with ethylene

Due to the high selectivity towards small-diameter SWCNTs shown by ethylene, it was used in subsequent experiments to probe the diameter distributions of SWCNTs grown on Co and Co-Ru. SWCNT samples obtained using ethylene as a feedstock were further characterized ex situ by multi-excitation Raman spectroscopy (Figure 5). Green shades are added to the spectra to indicate the RBM frequencies corresponding to small diameter (< 1nm) SWCNTs. Figures 5a and 5b highlight the difference in RBM frequencies and intensities for SWCNTs grown on Co and Co-Ru with ethylene precursor. Interestingly, for each pair of SWCNT spectra on Co and Co-Ru acquired with the same excitation energy, there is an increase in the number of RBM peaks observed at higher frequencies for SWCNTs grown on Co-Ru catalyst. In addition, RBM peaks with the same frequency in the shaded region with diameters < 1 nm for the same excitation wavelength are characterized by different intensities, with SWCNTs grown on Co-Ru exhibiting a higher intensity. For instance, in Figure 5a, there is a weak intensity peak at ~300 cm^{-1} in the spectrum collected with 785 nm excitation, however in Figure 5b, the peak becomes prominent—an observation that occurs simultaneously with the disappearance of the peak at ~150 cm^{-1}. In the spectra acquired with the 633 nm laser, there is substantial increase in the intensities of peaks at ~255 cm^{-1} and ~285 cm^{-1}, relative to the peaks below 250 cm^{-1}. A similar trend is observed for spectra acquired with the 514 nm laser. Although there were no observable RBMs below 250 cm^{-1} for spectra acquired with the 1064 nm laser, peaks that appear above 300 cm^{-1} exhibit substantial increase in intensity. Multi-excitation Raman spectra for growth experiments using acetylene are shown in Figure S8. Ru appears to increase the selectivity of small-diameter SWCNTs by decreasing the relative amount of large-diameter SWCNTs and increasing the relative amount of small-diameter SWCNTs, evidenced by the reduced intensities

of RBM peaks associated with large-diameter SWCNTs and increased intensities of those associated with small-diameter SWCNTs (Figures 5 and S8).

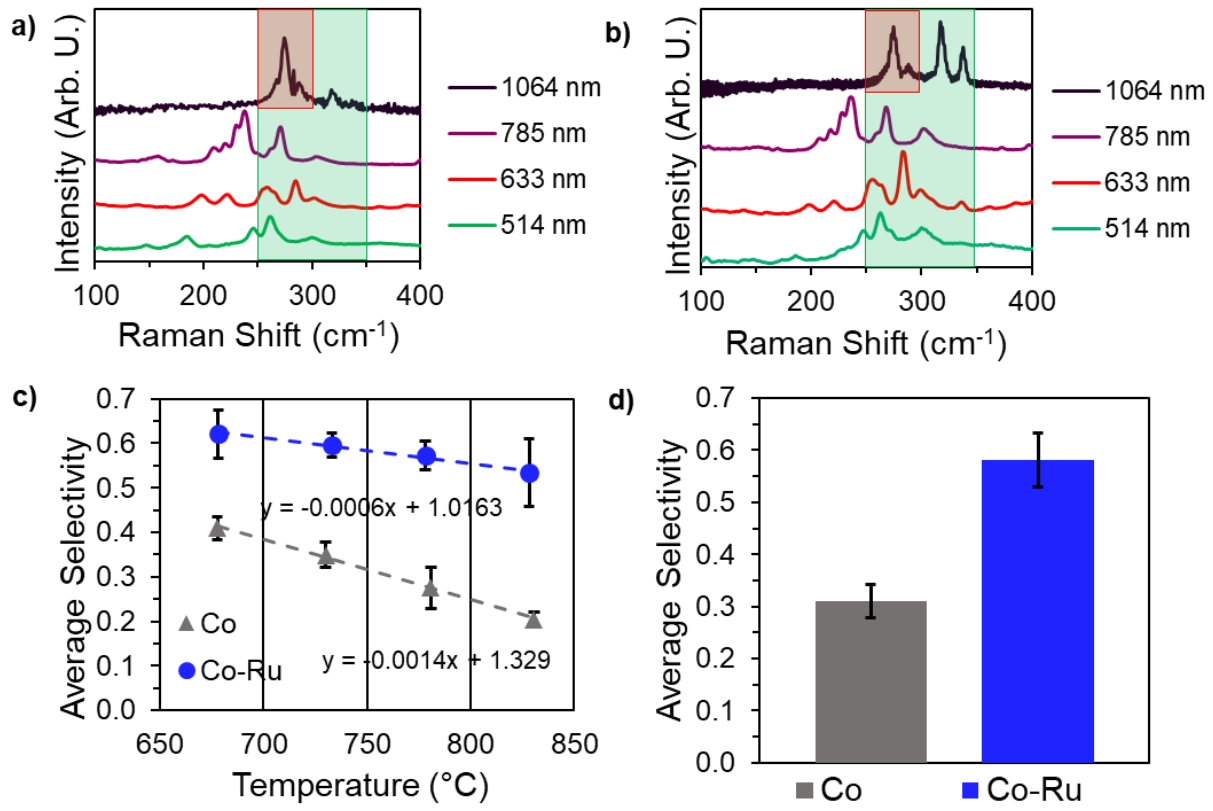

Figure 5. *Multi-excitation Raman spectra of SWCNTs grown on Co (a) and Co-Ru (b) catalysts; green shade highlights the small-diameter region (<1 nm). (c) Plots of selectivity averages for small-diameter SWCNTs on Co and Co-Ru catalysts. Data used for analysis were acquired with 532 nm and 633 nm laser excitations over four temperature ranges (650-699 °C, 700-749 °C, 750-799 °C, 800-849°C). (d) Histogram of average selectivity across temperature ranges for Co and Co-Ru catalysts. Error bars show standard deviations for the calculated average values.*

The plots in Figure 5 (c) clearly show the difference in selectivity toward small SWCNT diameters for Co and Co-Ru catalysts as a function of growth temperature, calculated by averaging selectivity data from Raman spectra acquired with 532 nm and 633 nm laser

excitations. The separated statistical analysis and trends for data obtained using the two laser excitations are shown in Figure S9. An important takeaway from the analysis is not only that the Co-Ru catalyst leads to higher selectivity for small-diameter SWCNTs at all growth temperatures investigated, but it is also less dependent on temperature. In fact, Co-Ru catalyst experiences minimal decrease in selectivity even in the highest temperature range (800 - 850°C). In contrast, Co catalyst experiences substantial drop-off in selectivity as temperature increases. The average selectivity values combined over all the growth temperatures are plotted in Figure 5 (d) and show that Ru as a catalyst promoter nearly doubles the selectivity of small-diameter SWCNTs. Our previous work revealed that catalyst activity during SWCNT growth is sensitive to the porosity or type of alumina (based on the deposition technique).[73] To understand the effect of alumina substrate porosity on catalyst behavior, we conducted additional experiments using Co and Co-Fe catalysts supported on IBS/e-deposited alumina films (with higher porosity) of the same thickness (10 nm) and the results (summarized in Figures S11-S14) are consistent with those discussed so far for catalysts supported on ALD-deposited alumina films.

3.3. DFT calculations

To understand the promotion role of Ru in increasing selectivity toward growth of small-diameter SWCNTs, we investigated the stability of Co and bimetallic Co_XRu_Y clusters using DFT calculations. These calculations focused on 13- and 55-atom clusters due to the high stability and symmetry of their structures, with sizes relevant to our experiments ((less than 1 nm). The Ru content of these clusters is similar to those used in the ARES experiments (which is 10%), with content ranging between 8% and 11% from the 13- and 55-atom cases, respectively ($Co_{12}Ru$ and $Co_{49}Ru_6$). However, to elucidate trends, calculations on pure Co clusters (Co_{13} and

Co_{55}), as well as on clusters with higher Ru content ($Co_{43}Ru_{12}$) were also performed. To obtain the cohesive energy, E_C, we used:

$$E_C = \frac{E_{cluster} - N_{Co}E_{Co} - N_{Ru}E_{Ru}}{N_{Co} + N_{Ru}} \quad (3)$$

The set of calculations on the 13-atom clusters are shown in Figure 6a, which shows the strengthening of cluster cohesive energy upon the addition of Ru. Specifically, the cohesive energy of the $Co_{12}Ru$ (8% Ru content) is 0.1 eV stronger than for Co_{13} (-3.4 eV for $Co_{12}Ru$ vs -3.3 eV for Co_{13}), which is expected to engender an increase in melting temperature and a reduction in atom mobility. While the stability of the $Co_{12}Ru$ cluster is slightly sensitive to the positioning of the Ru atom in the cluster, notice that the abovementioned strengthening of the cohesive energy occurs irrespective of whether the Ru atom is on the surface of the cluster ($Co_{12}Ru|_A$) or in the bulk ($Co_{12}Ru|_B$).

The set of calculations on the 55-atom clusters is shown in Figure 6b, which also shows the strengthening of cluster cohesive energy upon the addition of Ru. Specifically, the cohesive energy of $Co_{49}Ru_6$ (roughly 11% Ru) is around 0.2 eV stronger than for Co_{55}. Similar to the 13-atom cluster case, the stability of the 55-atom cluster is slightly sensitive to the exact arrangement of Ru atoms within the cluster. Yet, upon evaluation of six different configurations, the strengthening of the cohesive energy was similar, suggesting the robustness of the effect. To further confirm the trend of cohesive energy strengthening with Ru addition, we optimized a

$Co_{43}Ru_{12}$ cluster (~22% Ru content). The cohesive energy was found to strengthen a further 0.2 eV upon the addition of six more Ru atoms.

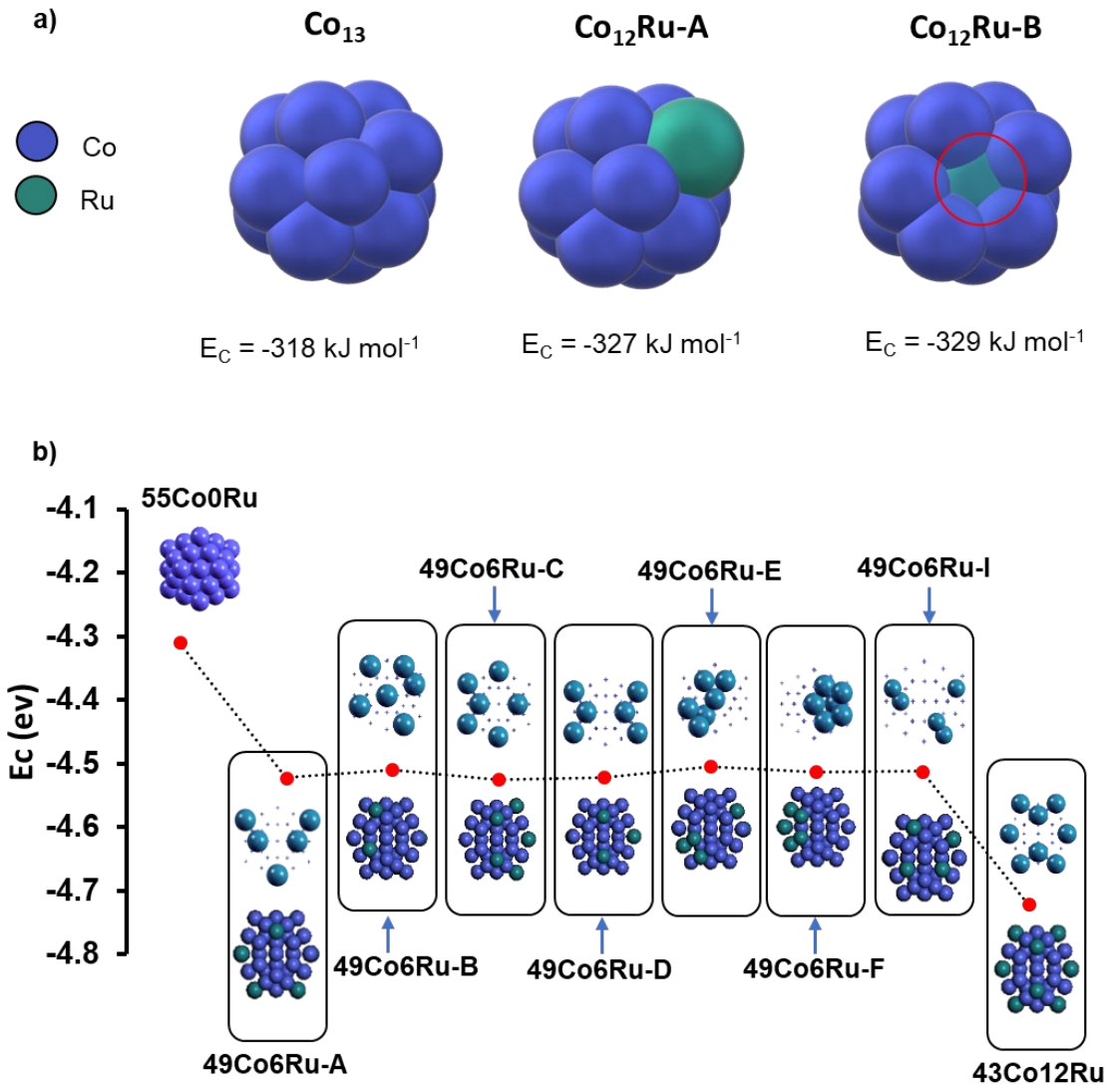

Figure 6. *(a) DFT optimization and calculation of cohesive energy, E_C, for13- and 55-atom clusters of Co and Co-Ru. a) Co13, Co12Ru (A) with adsorbed Ru atom, and Co12Ru (B) with Ru atom in the bulk region of the cluster. (b) Co55, Co49Ru6 (A-F), Co43Ru12, which contain 0, 6, and 12 Ru atoms, respectively. Configurations A through I were generated randomly and represent different arrangement scenarios for Ru on the cluster surface. Notably A represents the arrangement with the Ru atoms most separated from each other, D represents the arrangement with most symmetric Ru atom placement, and F represents the most segregated arrangement (notice all Ru atoms clustering together).*

Based on the above calculations, it appears Ru addition consistently increases the cohesive energy of the cluster—at least within the ranges experimentally tested—and that strengthening occurs by about the same magnitude regardless of the exact Ru distribution within the cluster. The results from these calculations are thus supportive of an increase in melting point and reduction in atom mobility, which should increase the resistance to catalyst sintering. We hypothesize the latter results in enhanced stability of small nanoparticles, which leads to higher selectivity of small-diameter SWCNTs.

3.4. SWCNT growth in ARES using pure Ru or Co-Ru with a higher Ru amount

To develop a deeper understanding of the catalytic properties of Ru, we conducted further experiments with pure Ru as a catalyst and a higher amount of Ru in Co-Ru catalysts and the results are summarized in Figure 7. We note that growth on pillars with a 1-nm-thick catalyst containing 20% Ru under conditions identical to those used for Co and Co-Ru (10% Ru) did not appear to yield SWCNTs, due to the absence of RBMs in their Raman spectra (Figure 7a). The results are likely related to the catalytic activity of the particles and not their stability, suggesting there might be an optimal amount of Ru in Co catalyst that supports good SWCNT growth, above which SWCNT growth might be inhibited. It is also possible SWCNT growth did not occur on Co-Ru (20% Ru) because the standard conditions used were optimum for pure Co and Co-Ru (10% Ru), not Co-Ru with higher Ru amount (20% Ru). To test this conjecture, we implemented the 'supergrowth' approach,[48, 74] well known for dramatically enhancing catalyst activity and lifetime[73, 75-76] during CVD growth. Interestingly, upon introduction of ~11ppm H_2O, Co-Ru (20% Ru) that was inactive for SWCNT growth under standard conditions as shown in Figure 7a, exhibited exceptional SWCNT growth (Figure 7b); however, the selectivity towards small-diameter SWCNTs was comparable to that observed with Co catalyst.

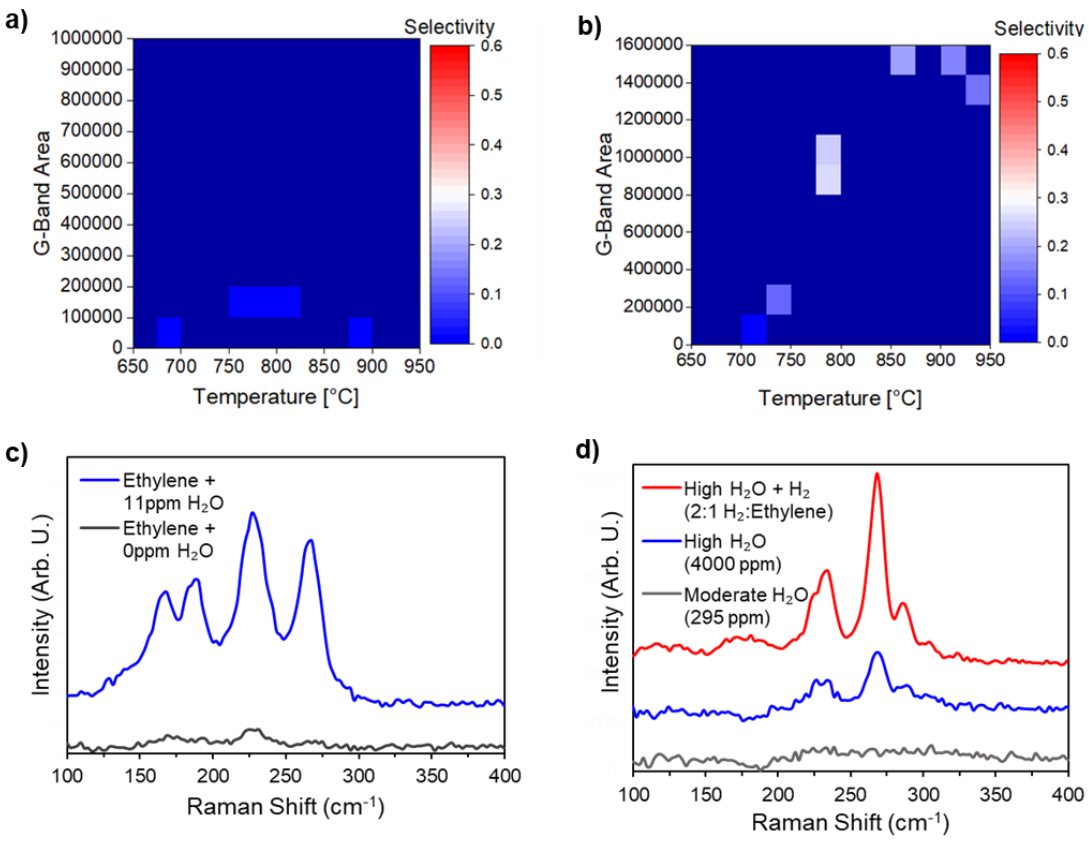

Figure 7. *Heat plots of G-band intensity and small diameter SWCNT selectivity of growth experiments performed on a Co-Ru catalyst (20% Ru) with ethylene and the addition of 0 ppm (a) and 11ppm H_2O (b). (c) Representative Raman spectra of SWCNTs grown on pure Ru catalyst with ethylene in the absence and presence of water (11 ppm). (d) Representative Raman spectra of SWCNTs grown on pure Ru catalysts under conditions that maximize small-diameter SWCNT selectivity.*

For comparison, we also conducted growth on pure Ru and the results are presented in Figures 7c and d. Little to no growth was observed even at a moderate water concentration (295 ppm). At extremely high-water concentrations (4000 ppm), growth of small-diameter SWCNTs occurred, although the total yield was extremely low (integrated G-band area < 7.0×10^4). Further optimization revealed that introducing a hydrogen-to-ethylene ratio of 2:1 yielded small-diameter

SWCNTs at ratios comparable to that obtained on Co-Ru (10% Ru). It should be noted, however, that growth on pure Ru required higher temperatures (900 - 950°C). Our results indicate that a high-melting-point metal like Ru in its pure form or as a promoter can generate small-diameter SWCNTs under optimum temperature and feedstock conditions.

4. Discussion

The Co-Ru catalyst nanoparticles formed by annealing the deposited films (a Ru layer on top of a Co layer) show higher selectivity toward small-diameter SWCNTs. Based on the DFT results, we hypothesize the presence of Ru in Co catalysts stabilizes small catalyst nanoparticles or suppresses sintering, resulting in a higher number density of small catalyst nanoparticles and a lower average catalyst size. To understand the role of Ru in catalyst evolution, similar as-deposited and annealed Co (1 nm) and Co-Ru (0.9 nm Co, 0.1 nm Ru) films on silicon substrates with alumina underlayers were studied; annealing was performed at 850°C in Ar/H_2 for 3, 10, and 30 min using a conventional CVD. AFM topographic profiles of the catalysts (Figure S10) reveal the average RMS roughness (proxy for feature height)[77-78] formed on Co-Ru is slightly lower than that of Co. The Co-Ru nanoparticles with smaller sizes nucleate SWCNTs with a much higher selectivity toward small-diameters and exhibit diminished overall SWCNT yield in comparison to pure Co. Even though FTS-GP exhibits relatively lower selectivity towards small-diameter SWCNTs, the promotion of Co with Ru leads to growth of small-diameter SWCNTs, affirming the key role Ru plays in the nucleation of small-diameter SWCNTs. We speculate the low yield observed for growth with FTS-GP on Co catalyst may be due to a number of reasons including on-site generation of water[25, 44] and the high-volume fraction of methane in FTS-GP. The water generated in situ via a reaction between H_2 and CO may etch some small-diameter

SWCNTs during nucleation or growth.[79-82] Gas phase reactions in ARES are extremely low or nonexistent because it relies on heating from the laser. We therefore expect the utilization of methane, a stable hydrocarbon and a major component (30 vol%) of FTS-GP, to be poor, thus limiting the carbon flux to the catalyst and contributing to growth inhibition. In consistent with this observation, we observed lower growth rate with FTS-GP in ARES.[44] When Ru is added to Co as a promoter, nucleation of small-diameter SWCNTs occurs with FTS-GP as a feedstock, despite the oxidizing environment that is created by water generation, for two reasons: (1) There is an increased number of small nanoparticles available for nucleation; and (2) Ru acts as an electron donor, which may protect SWCNTs from oxidation during nucleation.

The high variability observed in selectivity of small-diameter SWCNTs for Co-Ru may be due to the resulting catalyst nanoparticles not having equal amounts of Ru. It is unlikely the intended one-atom thick layer of Ru obtained via ion beam sputtering was uniform across the entire substrate. Possible clustering of Ru during deposition is expected to yield Co-Ru particles with slightly different Ru amounts in the nanoparticles after dewetting and particle formation, a phenomenon that has also been observed in Mo-on-Fe type catalysts.[83] The nonuniform amounts of Ru in the resulting Co-Ru catalyst particles may cause a variation in their catalytic activity, possibly due to the difference in their carbon solubility. Based on the DFT calculations, AFM characterization of annealed catalyst films, and growth in ARES, a mechanistic understanding of the role of Ru as a promoter of Co catalyst for SWCNT growth begins to take shape. As discussed earlier, DFT calculations indicate the inclusion of Ru atoms in a Co cluster increases cohesive energy, suggesting that smaller catalyst particles may be more resistant to sintering on a support. AFM analysis of annealed catalyst films reveals dewetted catalyst particles are smaller in the case of Co-Ru compared to pure Co, even at shorter time scales (3 min). The results

support the idea that Ru stabilizes Co nanoparticles, resulting in growth of small-diameter SWCNTs. In general, catalyst sintering is strongly dependent on temperature. Interestingly SWCNT size in the case of the Co-Ru catalyst is much less dependent on temperature as opposed to SWCNTs grown on pure Co. Our results indicate that the high melting point of Ru may be responsible for the increased cohesive energy and subsequent catalyst stability observed under SWCNT growth conditions.

5. Conclusions

In this work, rapid experimentation was used to probe favorable conditions that promote selective growth of small-diameter SWCNTs via catalytic CVD. To minimize Co catalyst size and enhance resistance to sintering, a high-melting-point metal (Ru) was used as a promoter of Co catalyst. The addition of 10% Ru to a 1-nm thick Co (Co-Ru) catalyst increases the selectivity of small-diameter SWCNTs, as calculated from Raman spectra collected using 532-nm and 633-nm laser excitations. In addition, Ru appears to stabilize catalyst particle size at elevated temperatures, as selectivity towards small-diameter SWCNTs is less temperature dependent for growth on Co-Ru compared to Co. The results are supported by AFM data on annealed catalyst films, which show slightly lower catalyst particle height on Co-Ru compared to Co for time-scales representative of SWCNT growth in ARES. The reduction in catalyst particle sintering has been attributed to an increase in cohesive energy in Co particles when Ru atoms are included in the cluster, as calculated by DFT for 13-atom and 55-atom clusters. Growth on Co-Ru resulted in lower overall SWCNT nucleation density compared to Co, whereas growth rates on Co-Ru were higher than growth on Co, with lifetimes roughly three times shorter than those for growth on Co. Furthermore, our results reveal that pure Ru or Co-Ru with a higher Ru amount can support growth of small-diameter SWCNTs under optimum temperature and water

concentration. The study reveals important relationships between catalyst promotion using Ru, type of feedstock, SWCNT diameter, and growth temperature. These findings highlight the role of Ru as a promoter of Co and as a catalyst in the growth of small-diameter SWCNTs, which opens the door for future applications requiring small-diameter SWCNTs.

Supporting Information

Representative Raman spectra and peak fitting for SWCNTs grown catalysts; analysis of Raman spectra acquired using multi-excitation wavelengths; small-diameter SWCNT selectivity data separated on the basis of excitation wavelength showing the effects of type of feedstock, growth temperature, and catalyst promotion on SWCNT growth (yield and small-diameter selectivity); AFM data of as-deposited and annealed catalyst films; small-diameter SWCNT **s**electivity data for catalysts supported on IBS/e alumina; and analysis of C_1 and C_2 values in Equation 1. The Supporting Information is available free of charge *via* the Internet at http://pubs.acs.org.

Notes

The authors declare no competing interest.

Acknowledgements

The research was supported by the National Science Foundation (Grant No. 1653527) and the Air Force Research Laboratory. D.A.G.-G. acknowledges funding from NSF (CBET-1921484) and computational resources from the Mio supercomputer cluster at Colorado School of Mines

References

1. Franklin, A. D.; Luisier, M.; Han, S.-J.; Tulevski, G.; Breslin, C. M.; Gignac, L.; Lundstrom, M. S.; Haensch, W., Sub-10 nm Carbon Nanotube Transistor. *Nano Letters* **2012,** *12* (2), 758-762.

2. Qiu, C.; Zhang, Z.; Xiao, M.; Yang, Y.; Zhong, D.; Peng, L.-M., Scaling carbon nanotube complementary transistors to 5-nm gate lengths. *Science* **2017,** *355* (6322), 271.

3. Yan, H.; Choe, H. S.; Nam, S.; Hu, Y.; Das, S.; Klemic, J. F.; Ellenbogen, J. C.; Lieber, C. M., Programmable nanowire circuits for nanoprocessors. *Nature* **2011,** *470* (7333), 240-244.

4. Zhang, L.; Zaric, S.; Tu, X.; Wang, X.; Zhao, W.; Dai, H., Assessment of Chemically Separated Carbon Nanotubes for Nanoelectronics. *Journal of the American Chemical Society* **2008,** *130* (8), 2686-2691.

5. Miyata, Y.; Shiozawa, K.; Asada, Y.; Ohno, Y.; Kitaura, R.; Mizutani, T.; Shinohara, H., Length-sorted semiconducting carbon nanotubes for high-mobility thin film transistors. *Nano Research* **2011,** *4* (10), 963-970.

6. Cao, Q.; Kim, H.-s.; Pimparkar, N.; Kulkarni, J. P.; Wang, C.; Shim, M.; Roy, K.; Alam, M. A.; Rogers, J. A., Medium-scale carbon nanotube thin-film integrated circuits on flexible plastic substrates. *Nature* **2008,** *454* (7203), 495-500.

7. Park, S.; Vosguerichian, M.; Bao, Z., A review of fabrication and applications of carbon nanotube film-based flexible electronics. *Nanoscale* **2013,** *5* (5), 1727-1752.

8. Lefebvre, J.; Ding, J.; Li, Z.; Finnie, P.; Lopinski, G.; Malenfant, P. R. L., High-Purity Semiconducting Single-Walled Carbon Nanotubes: A Key Enabling Material in Emerging Electronics. *Accounts of Chemical Research* **2017,** *50* (10), 2479-2486.

9. Jiang, S.; Hou, P.-X.; Chen, M.-L.; Wang, B.-W.; Sun, D.-M.; Tang, D.-M.; Jin, Q.; Guo, Q.-X.; Zhang, D.-D.; Du, J.-H.; Tai, K.-P.; Tan, J.; Kauppinen, E. I.; Liu, C.; Cheng, H.-M., Ultrahigh-performance transparent conductive films of carbon-welded isolated single-wall carbon nanotubes. *Science Advances* **2018,** *4* (5), eaap9264.

10. Asada, Y.; Nihey, F.; Ohmori, S.; Shinohara, H.; Saito, T., Diameter-Dependent Performance of Single-Walled Carbon Nanotube Thin-Film Transistors. *Advanced Materials* **2011,** *23* (40), 4631-4635.

11. Cao, Q.; Han, S.-j.; Tulevski, G. S.; Zhu, Y.; Lu, D. D.; Haensch, W., Arrays of single-walled carbon nanotubes with full surface coverage for high-performance electronics. *Nature Nanotechnology* **2013,** *8* (3), 180-186.

12. Landi, B. J.; Ganter, M. J.; Cress, C. D.; DiLeo, R. A.; Raffaelle, R. P., Carbon nanotubes for lithium ion batteries. *Energy Environ. Sci.* **2009,** *2* (6), 638-654.

13. Kaempgen, M.; Chan, C. K.; Ma, J.; Cui, Y.; Gruner, G., Printable Thin Film Supercapacitors Using Single-Walled Carbon Nanotubes. *Nano Letters* **2009,** *9* (5), 1872-1876.

14. Kim, B.; Chung, H.; Kim, W., High-performance supercapacitors based on vertically aligned carbon nanotubes and nonaqueous electrolytes. *Nanotechnology* **2012,** *23* (15), 155401.

15. Li, M.; Carter, R.; Douglas, A.; Oakes, L.; Pint, C. L., Sulfur Vapor-Infiltrated 3D Carbon Nanotube Foam for Binder-Free High Areal Capacity Lithium–Sulfur Battery Composite Cathodes. *ACS Nano* **2017,** *11* (5), 4877-4884.

16. Blackburn, J. L., Semiconducting Single-Walled Carbon Nanotubes in Solar Energy Harvesting. *ACS Energy Letters* **2017,** *2* (7), 1598-1613.

17. Habisreutinger, S. N.; Leijtens, T.; Eperon, G. E.; Stranks, S. D.; Nicholas, R. J.; Snaith, H. J., Enhanced Hole Extraction in Perovskite Solar Cells Through Carbon Nanotubes. *The Journal of Physical Chemistry Letters* **2014,** *5* (23), 4207-4212.

18. Odom, T. W.; Huang, J.-L.; Lieber, C. M., STM studies of single-walled carbon nanotubes. *Journal of Physics: Condensed Matter* **2002,** *14* (6), R145-R167.

19. Matsuda, Y.; Tahir-Kheli, J.; Goddard, W. A., Definitive Band Gaps for Single-Wall Carbon Nanotubes. *The Journal of Physical Chemistry Letters* **2010,** *1* (19), 2946-2950.

20. Cheung, C. L.; Kurtz, A.; Park, H.; Lieber, C. M., Diameter-controlled synthesis of carbon nanotubes. *Journal of Physical Chemistry B* **2002,** *106* (10), 2429-2433.

21. Li, Y.; Kim, W.; Zhang, Y.; Rolandi, M.; Wang, D.; Dai, H., Growth of single-walled carbon nanotubes from discrete catalytic nanoparticles of various sizes. *Journal of Physical Chemistry B* **2001,** *105* (46), 11424-11431.

22. Chen, Z.; Kim, D. Y.; Hasegawa, K.; Noda, S., Methane-Assisted Chemical Vapor Deposition Yielding Millimeter-Tall Single-Wall Carbon Nanotubes of Smaller Diameter. *ACS Nano* **2013,** *7* (8), 6719-6728.

23. Hata, K.; Futaba, D. N.; Mizuno, K.; Namai, T.; Yumura, M.; Iijima, S., Water-Assisted Highly Efficient Synthesis of Impurity-Free Single-Walled Carbon Nanotubes. *Science* **2004,** *306* (5700), 1362-1364.

24. Sakurai, S.; Inaguma, M.; Futaba, D. N.; Yumura, M.; Hata, K., A Fundamental Limitation of Small Diameter Single-Walled Carbon Nanotube Synthesis—A Scaling Rule of the Carbon Nanotube Yield with Catalyst Volume. *Materials* **2013,** *6* (7), 2633-2641.

25. Almkhelfe, H.; Li, X.; Rao, R.; Amama, P. B., Catalytic CVD growth of millimeter-tall single-wall carbon nanotube carpets using industrial gaseous waste as a feedstock. *Carbon* **2017,** *116*, 181-190.

26. Zheng, M.; Jagota, A.; Strano, M. S.; Santos, A. P.; Barone, P.; Chou, S. G.; Diner, B. A.; Dresselhaus, M. S.; McLean, R. S.; Onoa, G. B.; Samsonidze, G. G.; Semke, E. D.; Usrey, M.; Walls, D. J., Structure-Based Carbon Nanotube Sorting by Sequence-Dependent DNA Assembly. *Science* **2003,** *302* (5650), 1545.

27. Arnold, M. S.; Green, A. A.; Hulvat, J. F.; Stupp, S. I.; Hersam, M. C., Sorting carbon nanotubes by electronic structure using density differentiation. *Nature Nanotechnology* **2006,** *1* (1), 60-65.

28. Liu, H.; Nishide, D.; Tanaka, T.; Kataura, H., Large-scale single-chirality separation of single-wall carbon nanotubes by simple gel chromatography. *Nature Communications* **2011,** *2* (1), 309.

29. Fagan, J. A.; Khripin, C. Y.; Silvera Batista, C. A.; Simpson, J. R.; Hároz, E. H.; Hight Walker, A. R.; Zheng, M., Isolation of Specific Small-Diameter Single-Wall Carbon Nanotube Species via Aqueous Two-Phase Extraction. *Advanced Materials* **2014,** *26* (18), 2800-2804.

30. Rao, R.; Pint, C. L.; Islam, A. E.; Weatherup, R. S.; Hofmann, S.; Meshot, E. R.; Wu, F.; Zhou, C.; Dee, N.; Amama, P. B.; Carpena-Nuñez, J.; Shi, W.; Plata, D. L.; Penev, E. S.; Yakobson, B. I.; Balbuena, P. B.; Bichara, C.; Futaba, D. N.; Noda, S.; Shin, H.; Kim, K. S.; Simard, B.; Mirri, F.; Pasquali, M.; Fornasiero, F.; Kauppinen, E. I.; Arnold, M.; Cola, B. A.; Nikolaev, P.; Arepalli, S.; Cheng, H.-M.; Zakharov, D. N.; Stach, E. A.; Zhang, J.; Wei, F.; Terrones, M.; Geohegan, D. B.; Maruyama, B.; Maruyama, S.; Li, Y.; Adams, W. W.; Hart, A. J., Carbon Nanotubes and Related Nanomaterials: Critical Advances and Challenges for Synthesis toward Mainstream Commercial Applications. *ACS Nano* **2018,** *12* (12), 11756-11784.

31. Gómez-Gualdrón, D. A.; Balbuena, P. B., Characterization of carbon atomistic pathways during single-walled carbon nanotube growth on supported metal nanoparticles. *Carbon* **2013,** *57*, 298-309.

32. Fiawoo, M. F. C.; Bonnot, A. M.; Amara, H.; Bichara, C.; Thibault-Pénisson, J.; Loiseau, A., Evidence of Correlation between Catalyst Particles and the Single-Wall Carbon Nanotube Diameter: A First Step towards Chirality Control. *Physical Review Letters* **2012,** *108* (19), 195503.

33. Bachilo, S. M.; Balzano, L.; Herrera, J. E.; Pompeo, F.; Resasco, D. E.; Weisman, R. B., Narrow (n,m)-Distribution of Single-Walled Carbon Nanotubes Grown Using a Solid Supported Catalyst. *Journal of the American Chemical Society* **2003,** *125* (37), 11186-11187.

34. Cao, A.; Veser, G., Exceptional high-temperature stability through distillation-like self-stabilization in bimetallic nanoparticles. *Nature Materials* **2010,** *9* (1), 75-81.

35. Romanenko, A. V.; Tyschishin, E. A.; Moroz, E. M.; Likholobov, V. A.; Zaikovskii, V. I.; Jhung, S. H.; Park, Y. S., Influence of ruthenium addition on sintering of carbon-supported palladium. *Applied Catalysis A: General* **2002,** *227* (1), 117-123.

36. Budiman, A. W.; Song, S. H.; Chang, T. S.; Choi, M. J., Preparation of a high performance cobalt catalyst for CO2 reforming of methane. *Advanced Powder Technology* **2016,** *27* (2), 584-590.

37. Wang, X.; Fu, X.-P.; Yu, W.-Z.; Ma, C.; Jia, C.-J.; Si, R., Synthesis of a ceria-supported iron–ruthenium oxide catalyst and its structural transformation from subnanometer clusters to single atoms during the Fischer–Tropsch synthesis reaction. *Inorganic Chemistry Frontiers* **2017,** *4* (12), 2059-2067.

38. Liu, X.; Zeng, J.; Shi, W.; Wang, J.; Zhu, T.; Chen, Y., Catalytic oxidation of benzene over ruthenium–cobalt bimetallic catalysts and study of its mechanism. *Catalysis Science & Technology* **2017,** *7* (1), 213-221.

39. Tanabe, K., Catalytic application of niobium compounds. *Catalysis Today* **2003,** *78* (1), 65-77.

40. Cui, X.; Xu, J.; Zhang, C.; Yang, Y.; Gao, P.; Wu, B.; Li, Y., Effect of pretreatment on precipitated Fe–Mo Fischer–Tropsch catalysts: Morphology, carburization, and catalytic performance. *Journal of Catalysis* **2011,** *282* (1), 35-46.

41. Phaahlamohlaka, T. N.; Dlamini, M. W.; Mogodi, M. W.; Kumi, D. O.; Jewell, L. L.; Billing, D. G.; Coville, N. J., A sinter resistant Co Fischer-Tropsch catalyst promoted with Ru and supported on titania encapsulated by mesoporous silica. *Applied Catalysis A: General* **2018,** *552*, 129-137.

42. Resasco, D. E.; Alvarez, W. E.; Pompeo, F.; Balzano, L.; Herrera, J. E.; Kitiyanan, B.; Borgna, A., A Scalable Process for Production of Single-walled Carbon Nanotubes (SWNTs) by Catalytic Disproportionation of CO on a Solid Catalyst. *Journal of Nanoparticle Research* **2002,** *4* (1), 131-136.

43. Cui, K.; Kumamoto, A.; Xiang, R.; An, H.; Wang, B.; Inoue, T.; Chiashi, S.; Ikuhara, Y.; Maruyama, S., Synthesis of subnanometer-diameter vertically aligned single-walled carbon nanotubes with copper-anchored cobalt catalysts. *Nanoscale* **2016,** *8* (3), 1608-1617.

44. Everhart, B. M.; Almkhelfe, H.; Li, X.; Wales, M.; Nikolaev, P.; Rao, R.; Maruyama, B.; Amama, P. B., Efficient Growth of Carbon Nanotube Carpets Enabled by In Situ Generation of Water. *Ind. Eng. Chem. Res.* **2020,** *59* (19), 9095-9104.

45. Almkhelfe, H.; Carpena-Nunez, J.; Back, T. C.; Amama, P. B., Gaseous product mixture from Fischer-Tropsch synthesis as an efficient carbon feedstock for low temperature CVD growth of carbon nanotube carpets. *Nanoscale* **2016,** *8* (27), 13476-13487.

46. Li, X.; Gray, E. R.; Islam, A. E.; Sargent, G. A.; Maruyama, B.; Amama, P. B., Magnesia and Magnesium Aluminate Catalyst Substrates for Carbon Nanotube Carpet Growth. *ACS Applied Nano Materials* **2020,** *3* (2), 1830-1840.

47. Nikolaev, P.; Hooper, D.; Perea-López, N.; Terrones, M.; Maruyama, B., Discovery of Wall-Selective Carbon Nanotube Growth Conditions via Automated Experimentation. *ACS Nano* **2014,** *8* (10), 10214-10222.

48. Futaba, D. N.; Hata, K.; Yamada, T.; Mizuno, K.; Yumura, M.; Iijima, S., Kinetics of Water-Assisted Single-Walled Carbon Nanotube Synthesis Revealed by a Time-Evolution Analysis. *Physical Review Letters* **2005,** *95* (5), 056104.

49. Rao, R.; Liptak, D.; Cherukuri, T.; Yakobson, B. I.; Maruyama, B., In situ evidence for chirality-dependent growth rates of individual carbon nanotubes. *Nature Materials* **2012,** *11* (3), 213-216.

50. Nikolaev, P.; Hooper, D.; Webber, F.; Rao, R.; Decker, K.; Krein, M.; Poleski, J.; Barto, R.; Maruyama, B., Autonomy in materials research: a case study in carbon nanotube growth. *npj Computational Materials* **2016,** *2* (1), 16031.

51. Kluender, E. J.; Hedrick, J. L.; Brown, K. A.; Rao, R.; Meckes, B.; Du, J. S.; Moreau, L. M.; Maruyama, B.; Mirkin, C. A., Catalyst discovery through megalibraries of nanomaterials. *Proc Natl Acad Sci U S A* **2019,** *116* (1), 40-45.

52. Rao, R.; Pierce, N.; Liptak, D.; Hooper, D.; Sargent, G.; Semiatin, S. L.; Curtarolo, S.; Harutyunyan, A. R.; Maruyama, B., Revealing the Impact of Catalyst Phase Transition on Carbon Nanotube Growth by in Situ Raman Spectroscopy. *ACS Nano* **2013,** *7* (2), 1100-1107.

53. Meshot, E. R.; Plata, D. L.; Tawfick, S.; Zhang, Y.; Verploegen, E. A.; Hart, A. J., Engineering Vertically Aligned Carbon Nanotube Growth by Decoupled Thermal Treatment of Precursor and Catalyst. *ACS Nano* **2009,** *3* (9), 2477-2486.

54. Kresse, G.; Hafner, J., Ab initio molecular dynamics for liquid metals. *Physical Review B* **1993,** *47* (1), 558-561.

55. Kresse, G.; Furthmüller, J., Efficiency of ab-initio total energy calculations for metals and semiconductors using a plane-wave basis set. *Computational Materials Science* **1996,** *6* (1), 15-50.

56. Kresse, G.; Furthmüller, J., Efficient iterative schemes for ab initio total-energy calculations using a plane-wave basis set. *Physical Review B* **1996,** *54* (16), 11169-11186.

57. Perdew, J. P.; Burke, K.; Ernzerhof, M., Generalized Gradient Approximation Made Simple. *Physical Review Letters* **1996,** *77* (18), 3865-3868.

58. Grimme, S., Semiempirical GGA-type density functional constructed with a long-range dispersion correction. *Journal of Computational Chemistry* **2006,** *27* (15), 1787-1799.

59. Blöchl, P. E., Projector augmented-wave method. *Physical Review B* **1994,** *50* (24), 17953-17979.

60. Kresse, G.; Joubert, D., From ultrasoft pseudopotentials to the projector augmented-wave method. *Physical Review B* **1999,** *59* (3), 1758-1775.

61. Ho, K. M.; Fu, C. L.; Harmon, B. N.; Weber, W.; Hamann, D. R., Vibrational Frequencies and Structural Properties of Transition Metals via Total-Energy Calculations. *Physical Review Letters* **1982,** *49* (9), 673-676.

62. Rodríguez-López, J. L.; Aguilera-Granja, F.; Michaelian, K.; Vega, A., Structure and magnetism of cobalt clusters. *Physical Review B* **2003,** *67* (17), 174413.

63. Rao, A. M.; Richter, E.; Bandow, S.; Chase, B.; Eklund, P. C.; Williams, K. A.; Fang, S.; Subbaswamy, K. R.; Menon, M.; Thess, A.; Smalley, R. E.; Dresselhaus, G.; Dresselhaus, M. S., Diameter-Selective Raman Scattering from Vibrational Modes in Carbon Nanotubes. *Science* **1997,** *275* (5297), 187-191.

64. Dresselhaus, M. S.; Dresselhaus, G.; Saito, R.; Jorio, A., Raman spectroscopy of carbon nanotubes. *Physics Reports* **2005,** *409* (2), 47-99.

65. Jorio, A.; Saito, R.; Hafner, J. H.; Lieber, C. M.; Hunter, M.; McClure, T.; Dresselhaus, G.; Dresselhaus, M. S., Structural (n, m) determination of isolated single-wall carbon nanotubes by resonant Raman scattering. *Phys Rev Lett* **2001,** *86* (6), 1118-21.

66. Henrard, L.; Hernández, E.; Bernier, P.; Rubio, A., van der Waals interaction in nanotube bundles: Consequences on vibrational modes. *Physical Review B* **1999,** *60* (12), R8521-R8524.

67. Strano, M. S., Probing Chiral Selective Reactions Using a Revised Kataura Plot for the Interpretation of Single-Walled Carbon Nanotube Spectroscopy. *Journal of the American Chemical Society* **2003,** *125* (51), 16148-16153.

68. Milnera, M.; Kürti, J.; Hulman, M.; Kuzmany, H., Periodic Resonance Excitation and Intertube Interaction from Quasicontinuous Distributed Helicities in Single-Wall Carbon Nanotubes. *Physical Review Letters* **2000,** *84* (6), 1324-1327.

69. Kuzmany, H.; Plank, W.; Hulman, M.; Kramberger, C.; Grüneis, A.; Pichler, T.; Peterlik, H.; Kataura, H.; Achiba, Y., Determination of SWCNT diameters from the Raman response of the radial breathing mode. *The European Physical Journal B - Condensed Matter and Complex Systems* **2001,** *22* (3), 307-320.

70. O'Connell, M. J.; Sivaram, S.; Doorn, S. K., Near-infrared resonance Raman excitation profile studies of single-walled carbon nanotube intertube interactions: A direct comparison of bundled and individually dispersed HiPco nanotubes. *Physical Review B* **2004,** *69* (23), 235415.

71. Telg, H.; Maultzsch, J.; Reich, S.; Hennrich, F.; Thomsen, C., Chirality Distribution and Transition Energies of Carbon Nanotubes. *Physical Review Letters* **2004,** *93* (17), 177401.

72. Maultzsch, J.; Telg, H.; Reich, S.; Thomsen, C., Radial breathing mode of single-walled carbon nanotubes: Optical transition energies and chiral-index assignment. *Physical Review B* **2005,** *72* (20), 205438.

73. Amama, P. B.; Pint, C. L.; Kim, S. M.; McJilton, L.; Eyink, K. G.; Stach, E. A.; Hauge, R. H.; Maruyama, B., Influence of Alumina Type on the Evolution and Activity of Alumina-Supported Fe Catalysts in Single-Walled Carbon Nanotube Carpet Growth. *ACS Nano* **2010,** *4* (2), 895-904.

74. Hata, K.; Futaba, D. N.; Mizuno, K.; Namai, T.; Yumura, M.; Iijima, S., Water-assisted highly efficient synthesis of impurity-free single-walled carbon nanotubes. *Science* **2004,** *306* (5700), 1362-4.

75. Amama, P. B.; Pint, C. L.; McJilton, L.; Kim, S. M.; Stach, E. A.; Murray, P. T.; Hauge, R. H.; Maruyama, B., Role of Water in Super Growth of Single-Walled Carbon Nanotube Carpets. *Nano Lett.* **2009,** *9* (1), 44-49.

76. Kim, S. M.; Pint, C. L.; Amama, P. B.; Zakharov, D. N.; Hauge, R. H.; Maruyama, B.; Stach, E. A., Evolution in catalyst morphology leads to carbon nanotube growth termination. *J. Phys. Chem. Lett.* **2010,** *1* (6), 918-922.

77. Zaitsev, B. N.; Baklanova, N. I.; Zima, T. M., Atomic force microscopy study of surface-modified carbon fibers. *Inorganic Materials* **2008,** *44* (6), 592-597.

78. Paik, P.; Kar, K. K., Surface roughness and morphology of polypropylene nanospheres: effects of particles size. *Surface Engineering* **2008,** *24* (5), 341-349.

79. Zhang, M.; Yudasaka, M.; Iijima, S., Diameter Enlargement of Single-Wall Carbon Nanotubes by Oxidation. *The Journal of Physical Chemistry B* **2004,** *108* (1), 149-153.

80. Borowiak-Palen, E.; Pichler, T.; Liu, X.; Knupfer, M.; Graff, A.; Jost, O.; Pompe, W.; Kalenczuk, R. J.; Fink, J., Reduced diameter distribution of single-wall carbon nanotubes by selective oxidation. *Chemical Physics Letters* **2002,** *363* (5), 567-572.

81. Dementev, N.; Osswald, S.; Gogotsi, Y.; Borguet, E., Purification of carbon nanotubes by dynamic oxidation in air. *Journal of Materials Chemistry* **2009,** *19* (42), 7904-7908.

82. Liao, Y.; Hussain, A.; Laiho, P.; Zhang, Q.; Tian, Y.; Wei, N.; Ding, E.-X.; Khan, S. A.; Nguyen, N. N.; Ahmad, S.; Kauppinen, E. I., Tuning Geometry of SWCNTs by CO2 in Floating Catalyst CVD for High-Performance Transparent Conductive Films. *Advanced Materials Interfaces* **2018,** *5* (23), 1801209.

83. Youn, S. K.; Park, H. G., Morphological Evolution of Fe–Mo Bimetallic Catalysts for Diameter and Density Modulation of Vertically Aligned Carbon Nanotubes. *The Journal of Physical Chemistry C* **2013,** *117* (36), 18657-18665.

Graphical Abstract